Estuaries and Coasts (2017) 40:343–358
DOI 10.1007/s12237-016-0164-3

Using Satellite Observations to Characterize the Response of Estuarine Turbidity Maxima to External Forcing

Austin S. Hudson[1] · **Stefan A. Talke**[1] · **David A. Jay**[1]

Received: 6 January 2016 / Revised: 28 August 2016 / Accepted: 4 September 2016 / Published online: 27 September 2016

Abstract This study explores the spatial and temporal character of turbidity maxima in the Columbia River Estuary (CRE) using satellite observations. Surface reflectance data measured by the Moderate Imaging Spectroradiometer (MODIS) were calibrated against in situ measurements of surface turbidity (R^2 = 0.85 for 205 measurements). More than 1500 satellite images from 2000 to 2015 were then conditionally sampled to explore the physical processes that drive the spatial distribution of the turbidity field. We find satellite measurements are able to describe seasonal, spring–neap, and spatial features of the estuarine turbidity maxima (ETM) that are not easily observable by other means. System-wide levels of turbidity are most sensitive to river flow and spring–neap tidal range, with a weaker correlation to wind and waves. Maximum surface turbidity is observed in winter during elevated flow from coastal tributaries and remains elevated during the spring freshet of the main stem Columbia. Two ETM with asymmetric along-channel profiles are observed, one in the North Channel and another in the South Channel. Turbidity distributions migrate downstream as tidal range and river flow increase but appear to become topographically trapped near topographic holes at river kilometers 15–20. Hence, depth-sensitive circulation processes like internal asymmetry and gravitational circulation are likely important mechanisms for trapping particles and determining ETM location. These conclusions confirm the theoretical result that along-channel distributions of turbidity should have an asymmetric distribution and emphasize the role of bottom topography.

Keywords Estuarine turbidity maxima · Remote sensing · MODIS · Columbia River Estuary

Communicated by Richard C. Zimmerman

✉ Austin S. Hudson
hudsona@pdx.edu

[1] Department of Civil and Environmental Engineering, Portland State University, PO Box 751 - CEE, Portland, OR 97207, USA

Introduction

Estuaries and the surrounding coastal environment are greatly influenced by sediment distribution and transport processes. Variations in river flow, tides, particle settling velocity, and bathymetry help control transport, deposition, and erosion patterns that shape the morphology of these regions (Meade 1969; Stevenson et al. 1985; Jay et al. 1990; Sherwood et al. 1990; Geyer et al. 2001; Elias et al. 2012). Since cohesive sediment particles also include nutrients, organic matter, and contaminants, the distribution of sediment also helps regulate ecological activity (Simenstad et al. 1990). For example, water column turbidity inhibits algae growth (e.g., May et al. 2003), such that the spatial distribution of turbidity helps set the spatial distribution of algal blooms (de Swart et al. 2009). Similarly, the minimum oxygen concentration is often found in the estuarine turbidity maximum (ETM) zone, due to the large concentration of organic material (e.g., Talke et al. 2009a).

Despite the importance of estuarine turbidity to system functioning, measuring and interpreting spatial patterns of turbidity remain challenging (Jay et al. 2015). Few estuaries have the well-developed, long-term in situ monitoring programs required to assess seasonal patterns and the spatial effects of tidal, riverine, and wind forcing (Jay et al. 2015). Logistics and costs limit the spatial resolution of in situ sensors. Moreover, in situ point data are inherently difficult to interpret when large spatial variability is present, since it becomes

difficult to separate vertical mixing processes from horizontal advection (i.e., the usual assumption that advective transport is small breaks down when large spatial gradients exist). To combat this deficiency, multiple studies starting with Postma and Kalle (1955) have analyzed the turbidity distribution measured from moving ships (see also Kappenberg and Grabemann 2001; Uncles et al. 2002; Talke et al. 2009a, b; de Jonge et al. 2014). While shipboard transects obtain better spatial resolution than in situ data, the measurements are often obtained over multiple hours or even a day, especially in long estuaries (Talke et al. 2008). Spatial measurements are therefore only quasi-synoptic and often occur at different tidal phases, depth, and mixing conditions. Hence, interpretation of the spatial distribution is affected or biased by ship travel time and temporal aliasing.

Satellite measurements offer an opportunity to address the limitations of in situ measurements by obtaining instantaneous snapshots of an estuary with much higher spatial resolution. A number of studies have developed methods for remotely measuring suspended sediment concentration (SCC) in estuarine environments using the MODerate Imaging Spectroradiometer (MODIS) and other satellite-based instruments (e.g., Ruhl et al. 2001; Doxoran et al. 2003, 2006, 2009; Lehner et al. 2004; Chen et al. 2006; Palacios et al. 2009). These studies qualitatively link spatial patterns of turbidity to tidal, fluvial, and atmospheric forcing, demonstrating the potential of satellites for monitoring ETM. However, these studies have typically analyzed only a few images, possibly because satellite measurements have a long return period (typically 1 day to 2 weeks) relative to tidal forcing and are affected by atmospheric conditions, such that as few as 10 % of images can be used. Hence, interpretation of results has been qualitative and the potential of using satellite data to statistically characterize estuarine turbidity has not yet been exploited. We address these issues by applying a "big data" approach and evaluating the entire ~15-year MODIS record. After applying quality flags and retaining only good quality images, we conditionally sample the resulting data set of >1500 images to quantify the effects of river discharge, greater diurnal tidal range, and wind forcing on the turbidity field. A seasonally varying climatology is produced, and the relative contributions of different tributary streams to turbidity variability are determined.

Beyond quantifying spatial statistics, satellite measurements may allow us to investigate aspects of the along-channel turbidity distribution that have been difficult to ascertain with shipboard measurements or in situ sensors. For example, Talke et al. (2008, 2009b) suggest that the longitudinal profile of an ETM is inherently asymmetrical, due to the different forcing mechanisms (river flow, estuarine circulation) which dominate transport on either side of the ETM. Differences in the particle size distribution along the estuarine salinity gradient may also cause asymmetry in the suspended sediment distribution between the two sides of an ETM. Longitudinal profiles of the ETM have been measured, but (as discussed above) such shipboard measurements are not truly synoptic. Moreover, such longitudinal profiles may not adequately assess lateral variability in SSC. Hence, previously observed features in a turbidity field (such as multiple surface ETM) could (in theory) be due to either unresolved lateral variability or temporal variations in along-channel tidal forcing. In this study, we analyze instantaneous transects of surface turbidity in the Columbia River Estuary (CRE) using satellite-based estimates to test the hypothesis that ETM are asymmetrical. We also investigate the existence of multiple ETM and examine the physical mechanisms driving the turbidity distribution by monitoring the spatial and temporal variability of the ETM.

Our investigation addresses the following questions: (1) what are the tidal, fluvial, and seasonal patterns of ETM in the Columbia River Estuary? (2) are multiple surface ETM visible from satellite data? (3) what is the shape of the ETM under different conditions?, and (4) which physical variables control ETM position and shape? Since satellite data are synoptic, they can reveal spatially resolved features that cannot effectively be measured by either ship-based experiments or existing moored observations. These spatial snapshots can then be compared to theoretical descriptions of the turbidity distribution to reveal which mechanisms control circulation and transport.

Setting and Methods

In the following section, we detail the geophysical characteristics of the Columbia River Estuary (Section 2.1), summarize data sources (Section 2.2), and describe how turbidity is obtained from satellite remote sensing data (Section 2.3).

Site Characterization

The CRE is a drowned river valley in which salinity intrudes from the ocean into the lower estuary via two primary channels (North and South). These channels are separated by sand flats and are bordered on their other side by either coastline or large, shallow embayments. The estuary channels and subtidal flats have a shallow aspect ratio, with depths rarely exceeding 15 m. In this study, the system is divided into three regions (Fig. 1): the lower estuary between river kilometer (Rkm) 0 and 20, where saltwater is nearly always present and mechanical energy is dominated by tidal and wave processes; a mid-estuary region (Rkm 20–30) which typically exhibits the largest salinity gradients observed in the system; and an upper estuary region (Rkm 30–45) where salinity is often absent but density gradients occasionally occur and affect the velocity field.

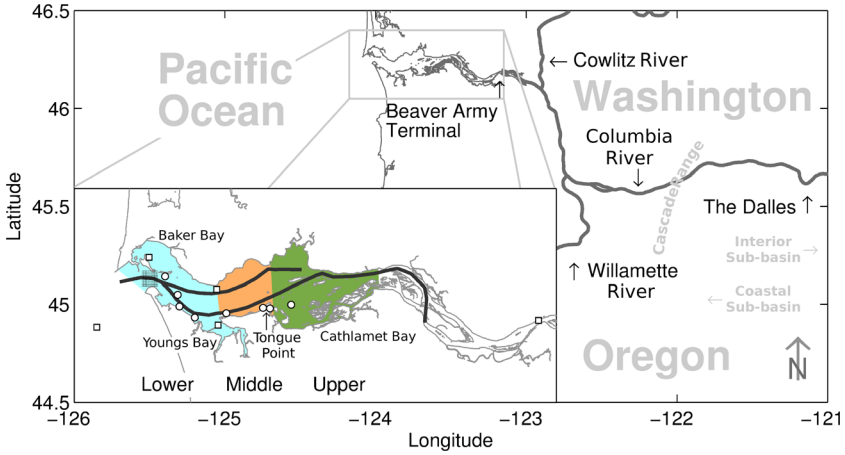

Fig. 1 The Columbia River, coastal tributaries (Cowlitz, Willamette, and Sandy), and Columbia River Estuary (*inset*). Columbia River flows are measured at The Dalles and Beaver Army Terminal. The lower estuary extends from the mouth (Rkm 0) to Young's Bay (~Rkm 15), mid-estuary continues up to Tongue Point (~Rkm 30), and the upper estuary to the landward limits of salinity intrusion (~Rkm 50). *Transects* denote the two main channels (North and South) in the system. Stations measuring turbidity are denoted by *square icons*, those measuring salinity by *circles*. Grid near mouth of Columbia River represents a 10 × 10 MODIS grid at 250-m resolution

Tides are mixed (predominately semidiurnal) with an M_2 amplitude that varies by ~10 % in the estuary, with a peak of 0.95 m near Rkm 30. Most of the tidal energy is focused in the lower and mid-estuary and begins decaying upstream due to bed roughness and river flow, despite cross-sectional convergence (Jay et al. 1990). The neap/spring cycle has a clear signal throughout the year with greater diurnal tidal range ranging from 1.6 to >3.6 m at Tongue Point. Tidal range is largest at the end of summer when the effect of river flow on tide wave propagation and attenuation is minimal (Jay 1984; Jay 1991; Chawla et al. 2007).

The Columbia is the largest Northeast Pacific river system, with a watershed of ~660,500 km^2. It is the source of 60 to 90 % of freshwater input to the coastal ocean of Northern California, Oregon, and Washington (Pruter and Alverson 1972). River flow exhibits strong seasonal variability, with the largest flows usually occurring during a May/June freshet. Much shorter winter freshets are fed primarily by coastal tributaries such as the Willamette and Cowlitz Rivers, while the smallest flows occur during late summer when precipitation and snowmelt runoff are minimal (Fig. 2). The annual regime of river flow has been dramatically altered by flow regulation and to a lesser extent climate change over the last century. Thus, contemporary spring freshet flows have been reduced by ~45 % and occur about a month earlier than their early twentieth century counterparts (Naik and Jay 2010; Naik and Jay 2011). This flow regulation has led to a decrease in sediment input from the main stem Columbia River, and the CRE is currently sediment-poor and erosional (Templeton and Jay 2013).

The residual (tidally averaged) estuarine circulation in the CRE is highly variable in space and time (Hughes and Rattray 1980; Jay and Smith 1990a). Irregular bottom topography (Fig. 3) augments spatial variability of the circulation by locally enhancing estuarine circulation, producing along-channel convergences and divergences in the residual flow, and intensifying or reducing vertical mixing (Jay and Smith 1990a). The salinity field transitions from weakly stratified (most of the tidal month) to strongly stratified conditions during and directly following neap tides (Jay and Smith 1990a, b). Flushing times and adjustments in the salinity field are relatively short (~few days) and nearly in phase with the spring–neap cycle and fluvial regime (Jay and Smith 1990a); therefore, scalar concentrations react quickly to changes in river flow, tides, and residual circulation.

Suspended sediment in the CRE is primarily of fluvial origin, composed mostly of fines (silt and clay) and aggregates, except during large tides and river flows when boundary shear stress is sufficient to suspend sands from the bed (Jay et al. 1990; Sherwood and Craeger 1990). Fines are supply limited; the capacity for transport is nearly always present and fine sediments will move whenever they are available. Coarse sediment (sand and gravel), in contrast, is transport capacity limited and there is an abundant supply that becomes mobile only under appropriate flow conditions (Naik and Jay 2011). Suspended sediment concentration (SSC) is typically less than 100 gm^{-3} throughout the CRE (Fain et al. 2001), a level much lower than in many other estuarine systems (Talke et al. 2009a, b; Doxaran et al. 2009). However, depth-averaged ETM sediment concentration can occasionally exceed 500 gm^{-3} (Gelfenbaum 1983).

Net sediment transport in the CRE is driven in part by tidally averaged estuarine circulation induced by horizontal density gradients (Hansen and Rattray 1965; Festa and Hansen 1978) and internal tidal asymmetry emerging from tidal modulations of vertical mixing and stratification (Jay and Smith 1990a; Simpson et al., 1990; Jay and Musiak, 1996; Burchard and Baumert 1998). Transport is also driven

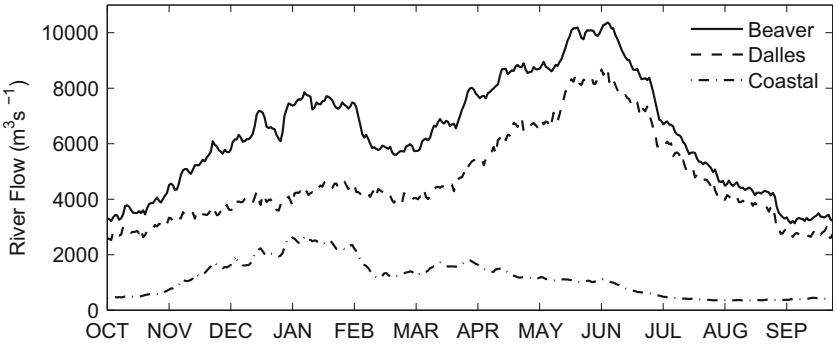

Fig. 2 Annual hydrograph measured at Beaver Army Terminal (the sum of all river flow entering the estuary; *solid line*), The Dalles (*dashed line*), and coastal tributaries (Willamette and Cowlitz rivers; *dash-dotted line*), monthly averaged during the study period in daily intervals. Maximum river flows in the Columbia River (The Dalles) are observed in May–June during the spring freshet; minimum flows occur during late summer. Coastal rivers peak during winter

by tidal asymmetries in flow and mixing caused by frictionally produced overtides (Geyer 1993; Jay and Musiak 1994, 1996; Burchard and Baumert 1998; Chernetsky et al. 2010; Burchard et al. 2013). Horizontal convergences in the residual and tidal sediment transport serve to trap particles and form ETM, the magnitude and location of which depends on the strength of the tides, river flow, stratification, and bottom topography (Geyer 1993; Jay and Musiak 1994; Burchard and Baumert 1998; Schoellhamer 2001; Talke et al. 2008; Donker and de Swart 2013).

ETM are found in both the North and South Channels of the CRE, in locations that are close to the upstream limits of salinity intrusion (Jay and Musiak 1994; Fain et al. 2001), though topographic lows in each channel appear to influence ETM position, as discussed below. The SSC in the ETM is up to ten times greater than the fluvial supply (Gelfenbaum 1983), though the residence time of sediment varies from a few days to several months (Fain et al. 2001). A third, more transient ETM has also been reported in association with the tidal intrusion fronts and a topographic low at about Rkm 5.

Data Sources and Processing

Satellite data used in this study are derived from surface reflectance measurements made by MODIS. Two versions of this instrument sample the CRE about 2 h apart near midday aboard the AQUA (2002 to present) and TERRA satellites (2000 to present). Data are available at various processing levels, ranging from raw data (level 0) to highly processed end products (level 3). Following Doxaran et al. (2009), a level 2 swath product (MOD09) processed by the Level 1 and Atmosphere Archive and Distribution System (LAADS; https://ladsweb.nascom.nasa.gov/) was used in this study. MOD09 is atmospherically corrected and includes state and quality datasets that flag pixels with clouds or cloud shadows, high or low aerosol concentrations, or that cover land and mark poor quality measurements. These flags were used to filter out measurements that incorrectly represent the state of the water surface. Remote turbidity estimates were calibrated using measurements from MODIS band 1 (620–670 nm) at a 250-m resolution (Fig. 1), chosen to resolve gradients in the estuary as well as possible.

In situ measurements of turbidity and salinity were derived from 13 stationary buoys (Tables 1 and 2 and Fig. 1) managed by the Center for Coastal Margin Observation and Prediction (CMOP; http://www.stccmop.org/datamart/). Turbidity observations used in this study were recorded intermittently from 2008 to 2015 (Fig. 4) at sub-minute intervals using WET Lab's ECO FLNTU (measuring at ~700 nm) or Turner Designs' Cyclops 7 (620–715 nm) fluorometers. Salinity measurements are available intermittently at various locations from 2003 to 2015. At each location, turbidity measurements are made within 2.5 m of the water surface. Data from the Saturn 01 profiling system in the North Channel (Table 1 and Fig. 1) were conditionally sampled and averaged over the top 2 m of the water column.

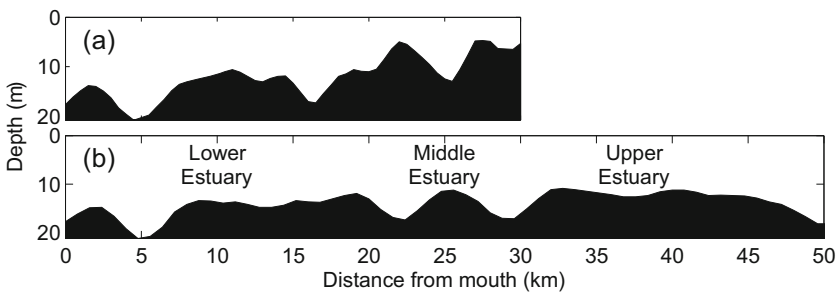

Fig. 3 Approximate depth profiles along the North (**a**) and South (**b**) Channel of the CRE, relative to MLLW. The South Channel is maintained at a minimum depth of 13 m, and both channels exhibit several topographic lows

Table 1 Locations of in situ turbidity measurements used in OLS

Buoy	Measurement Depth (m)	Latitude (deg)	Longitude (deg)
Saturn 01	–[a]	46.235	−123.872
Saturn 02	0–1	46.173	−124.127
Saturn 05	2.5	46.184	−123.188
Saturn 07	1	46.287	−124.016
Saturn 09	0.5	46.177	−123.869

[a] Measurements taken as an average over top 2 m of water column

Surface and near-bed salinity measurements at Saturn 01 in the North Channel (2008–2015) and Saturn 04 in the South Channel (2009–2015) were used to calculate salinity stratification. The along-channel salinity profile in the South Channel was parameterized using a hyperbolic tangent function, using a least squares fit of a hyperbolic tangent curve to salinity data following Warner et al. (2005) and Talke et al. (2009a, b):

$$S(x) = 0.5S_o\left(1-\tanh\frac{x-x_c}{x_L}\right) \quad (1)$$

where S_o is the ocean salinity and x_L and x_c are parameters that scale the salinity gradient and mark its maximum location, respectively. A least squares approach was applied to estimate x_c, x_L, and S_o, for near-bed measurements (data from 2003 to 2010) and near surface measurements (data from 2003 to 2006) to construct a salinity profile. The along-channel coordinate with 2 psu salinity was then used as marker for salinity intrusion. Data in the North Channel were too sparse to allow estimation of salinity intrusion.

Factors that affect turbidity include river discharge, tidal range, wind speed and direction, and ocean swell. These data are obtained from the United States Geological Survey (USGS) and National Oceanic and Atmospheric Administration (NOAA) and were recorded at various locations throughout the CRE (Table 3). River flow was processed as daily averages and all other measurements as hourly averages. Ocean swell was defined as the integrated spectral energy at frequencies <0.1 Hz (period $T \geq 10$ s), while wind speed was separated into two time series according to wind direction to take into account the effect of wind direction on wave fetch, following the approach of Talke and Stacey (2003). One wind speed time series consisted of wind blowing along the estuary axis from the west northwest (typical for summer conditions), while the other consisted of wind blowing from the east southeast, more typical of winter conditions.

The forcing variables—wind, waves, tides, and river discharge—were then regressed against MODIS-based surface turbidity estimates (described below) to determine the spatial zones of influence for each forcing variable. Other forcing variables are held approximately constant during each regression via a binning approach, to minimize the possibility that correlations are driven by another, jointly correlated process (such as seasonal changes in flow, wind, and tidal range). For example, we test the effect of wind direction and wave energy on turbidity by requiring that greater diurnal tidal range and river flow be in the range 2.5 ± 0.5 m and 5500 ± 1500 m^3 s^{-1}, respectively. These bin sizes are a compromise between holding forcing variables constant, to first order (20–30 % deviation from mean), while retaining enough samples to remain statistically significant. To account for the observation that erosion must occur over a critical stress, we further process the wind series by considering only wind speeds above a threshold. While empirical studies at other locations find a wind threshold of ~5–6 ms^{-1} for local erosion (e.g., de Jonge and van Beusekom 1995; Christie et al. 1999), we find

Table 2 Locations of in situ measurements used to derive salinity intrusion and stratification

Buoy	Measurement depth (m)	Latitude (deg)	Longitude (deg)	Distance from mouth (km)
SANDS	7.9	46.256	−123.982	7
DESD	7.3	46.226	−123.955	11
RED26	3.3	46.208	−123.951	12
TANSY	8.4	46.189	−123.919	15
Saturn 01	7.4	46.235	−123.872	16
MBS	2.6	46.196	−123.852	20
COAOF	2.1 or 3.2	46.205	−123.774	29
Saturn 04	8.6	46.204	−123.759	30
CBNC	6.5	46.210	−123.714	34

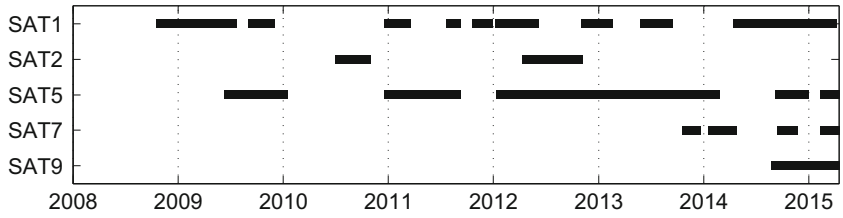

Fig. 4 Measurement record for turbidity sensors used in this study

that a lower threshold of 2 m/s obtains reasonable results while retaining a statistically significant sample size. The low threshold likely results from the presence of large mid-estuary flats and extensive peripheral bays. While the mid-estuary flats are primarily sand-bedded, they can temporarily retain fines (Sherwood and Craeger 1990).

Remote Sensing of Turbidity

Satellite-based instruments record *Top of the Atmosphere* (TOA) radiation, which is converted to surface reflectance (the ratio of reflected/backscattered radiance to incident solar irradiance) by adjusting raw measurements for solar and sensor zenith angles, gaseous and aerosol scattering and absorption, adjacency effects, and cloud contamination (cf. Vermote and Vermeulen 1999). Surface reflectance is measured in discrete frequency bands that correspond to peaks in the reflectance of various optically active constituents (OACs), such as suspended sediment or chlorophyll-*a*. Since the optical properties (e.g., absorption and backscatter spectra) of OACs change with concentration and significantly alter the measured reflectance signature (Bricaud et al. 1981; Bricaud et al. 1995; Neukermans et al. 2012), a relationship between satellite and in situ data can, in principle, be established.

Calibration of remote-based measurements of OACs is carried out by empirical or semi-analytical algorithms. Semi-analytical algorithms are based on modeling radiative transfer phenomena and rely on the deconvolution of the measured reflectance spectrum of a water body into individual OAC concentrations (Maritorena et al. 2002; IOCCG, 2006). By contrast, empirical algorithms rely on statistical correlations between remote and in situ data. They often involve band arithmetic formulae and have been successfully applied in various estuarine systems (Doxaran et al. 2003, 2006, 2009; Hu et al. 2004; Chen et al. 2006). Since OAC optical properties are not fully characterized in the CRE, semi-analytical methods applied to the Oregon coast typically fail in the estuary (Palacios et al. 2009). Therefore, we use an empirical model to derive satellite-based estimates of CRE surface turbidity.

The empirical model of surface turbidity was calibrated using a total of 205 concurrent measurements of turbidity and cloud-free surface reflectance during the observation period. To remove noise and small scale variability, in situ measurements were averaged over a 5-min period centered at the time of each satellite passing. MODIS data with a band 2-to-band 1 ratio >0.8 were excluded in the analysis. Ratios >0.8 correspond to land and cloud pixels missed in the MOD09 processing and proved useful for screening pixels which overlapped the shoreline and exposed sand flats.

MODIS and in situ data are significantly correlated (R^2 = 0.85, error variance = 1.25 ntu; Table 4 and Fig. 5), a relationship that most likely exists due to the proximity of the MODIS band 1 spectral range (620–670 nm) and the detection wavelength of the in situ turbidity sensors (~700 nm). Experimentation showed that a linear combination of band 1 and band 2 correlated slightly better with in situ data. Because this difference was not statistically significant, we use the simpler model based on band 1 only (Eq. 2 and Table 4). This calibration was then applied to more than 1500 images with good quality flags from the years 2000 to 2015.

$$\text{Turbidity} = 0.59 + 137 \times [\text{surface reflectance}] \quad (2)$$

Many sources of error can degrade the relationship between MODIS and in situ data, including (but not limited to)

Table 3 Measurement details of forcing parameters used in the analysis

Forcing	Measurement location
Wind speed/direction (m s^{-1}/deg)	NCDC (NOAA) Station 94224. Astoria Airport
Wave energy (m^2 Hz^{-1})	NBDC (NOAA) Station 46029. Columbia River Bar
Tidal range/elevation (m)	NOAA Station 9439040. Astoria, OR
River flow (m^3 s^{-1})	USGS 14246900. Columbia River. Beaver Army Terminal
	USGS 14243000. Cowlitz River. Castle Rock, WA
	USGS 14211720. Willamette River. Portland, OR
	USGS 14105700. Columbia River. The Dalles, OR

Table 4 Model statistics for OLS between band 1 and in situ turbidity and coefficient estimates

Model statistics			
Sample size	R^2	*P* value	Error variance
205	0.85	0	1.25 ntu
Coefficient estimated			
Intercept		Slope	
0.59 [0.38; 0.80]		137 [129; 145]	

Confidence intervals (a = 0.05) for coefficients are provided in brackets

atmospheric scattering, the presence of other OACs, the disparity between the in situ and remote detection wavelengths, reflectance off the bed in shallow regions, and land contamination for pixels near the shoreline. Furthermore, inherent differences in instrumentation and processing may also lead to errors in the model. Buoy observations are a point measurement that may not accurately assess spatial variability, whereas MODIS integrates variability in the top portion of the water column over a 250-m by 250-m area. Stratification in the water column, which is prevalent in the CRE, may augment depth-related discrepancies. However, the generally low error variance suggests that the sources of error described above do not significantly influence results within the turbidity maximum zone.

The contribution to surface reflectance of other OACs such as chlorophyll-*a* can also produce errors. Because primary production in the CRE is relatively low and the local food chain is predominantly detritus-based (Simenstad et al. 1990), we assume here that the most significant contribution to surface reflectance is suspended sediment. SSC obtained from spot water samples by the USGS at Beaver Army Terminal (Rkm 86) from 2010 to 2014 shows good agreement with in situ turbidity measurements made at the Saturn 05 station across the channel (data not shown; R^2 = 0.88, N = 21); hence, the assumption that surface reflectance and turbidity are dominated by suspended sediment (and not chlorophyll) appears appropriate to first order.

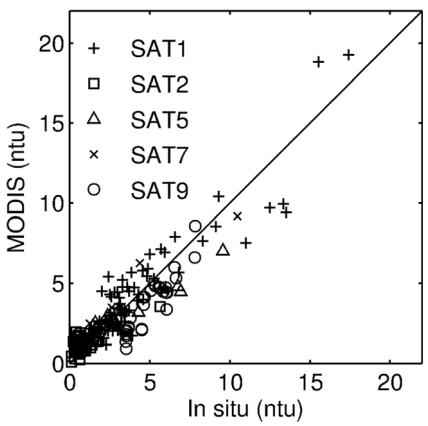

Fig. 5 Estimates of MODIS-based turbidity vs. in situ measurements

While we use estimates of turbidity as a proxy for sediment concentration, interpretation of in situ and remote turbidity estimates may be confounded by particle size variability in time and space. Since increased bed stresses during large tides and periods of strong current suspend larger particles from the bed, and since aggregation processes vary within an ETM and with tidal phase (Reed and Donovan 1994), turbidity/sediment calibrations which are sensitive to changes in particle size can undermine analysis of ETM behavior. Jay et al. (1999) found that calibrations of suspended particulate matter against acoustic backscatter varied over the tidal cycle in the CRE in response to changing scattering properties of different sized material. Nonetheless, Neukermans et al. (2012) found that WET Labs' optical sensors are driven to first order by particle concentrations, with a weaker, second-order dependence on particle size. Although this observation gives confidence in our calibration and interpretation of results, further research is required to definitively link sediment concentrations to our satellite-based turbidity estimates.

Results and Discussion

Next, we analyze seasonal patterns (Section 3.1) and along-channel distributions of MODIS-based surface turbidity (Section 3.2) in relation to external forcing variables.

Seasonal Turbidity Distribution

MODIS-based estimates of surface turbidity display a high degree of temporal and spatial variability. Four basic system states are shown in Fig. 6: low (3800 m^3 s^{-1}) vs high (12,000 m^3 s^{-1}) river flows during moderate tidal ranges (Fig. 6a, c) and neap (1.8 m) vs spring (3.5 m) tides during low river flow (Fig. 6b, d). As the source of most of the suspended sediment in the system (Jay et al. 1990), river flow has a direct relationship with surface concentrations throughout the estuary. Dependence on the neap/spring cycle is also apparent; greater concentrations are observed during spring tides when the larger tidal velocities mix sediment from the bed to the surface.

Monthly averaged turbidity fields in the estuary (Fig. 7) exhibit considerable seasonal variability during the study period; hence, the seasonally changing supply of sediment from the rivers is likely important. Maximum system-wide concentrations are observed in January and December during the winter rainy season, when considerable flow is input from tributaries west of the Cascade mountain range (daily average of ~2000 m^3 s^{-1}; Fig. 2), i.e., from the Coastal Sub-basin (Fig. 1; Naik and Jay 2011). Elevated turbidity levels persist throughout the spring freshet in May and June, with river flow measured at The Dalles averaging ~8000 m^3 s^{-1} and fed primarily by snowmelt in the Interior Sub-Basin. Both interior

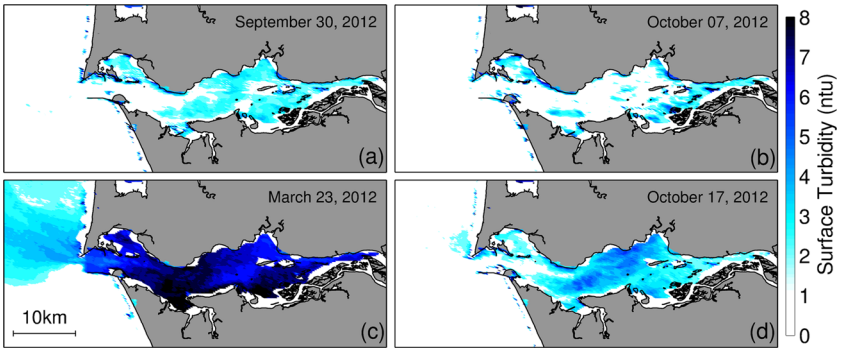

Fig. 6 Example turbidity distributions in the CRE derived from MODIS-based surface reflectance. The turbidity is a function of both river flow and tidal range. The *left panels* are measured at a time of moderate tidal ranges (~2.6 m) during low (**a**) and high (**c**) flow rates. *Right panels* illustrate neap (1.7 m tidal range) and spring (3.5 m tidal range; **b** and **d**, respectively) conditions at a time of low river flow. The *two plots* at bottom show prominent ETM

and coastal river flows subside during the summer dry season, reaching a minimum in September. The satellite-based climatology of turbidity (Fig. 7) is consistent with studies that show in situ sediment concentrations vary by a factor of 3 to 4 seasonally and up to 10 spatially (Gelfenbaum 1983; Sherwood and Craeger 1990; Fain et al. 2001). Figure 7 also suggests that the spatial distribution of monthly averaged turbidity is relatively constant and less variable than seasonal changes in concentration. Large gradients in the turbidity field are always present in the lower/mid-estuary, while gradients in the upper estuary are more muted.

Coastal turbidity patterns also exhibit seasonal variability. During winter months, a large coastal plume deflects northwards, consistent with in situ studies (Horner-Devine et al. 2009; Hickey et al. 2010) and the prevailing wind direction (see also Fig. 6). In upwelling conditions marked by northwesterly winds, the average turbidity is spread more symmetrically around the CRE mouth (e.g., June and July). During parts of the year (e.g., September), some estimates are below the noise floor (the error variance of the empirical model is 1.25 ntu; Table 4) and results are inconclusive.

The factors controlling the turbidity distributions in Fig. 6 and Fig. 7 are examined by correlating time series of river discharge, greater diurnal tidal range, estuarine wind speed, and offshore wave energy with corresponding estimates of surface turbidity at each pixel location (p value ≤ 0.01). Results suggest that turbidity is significantly correlated with along channel, summer wind speed (>2 ms^{-1}) in shallow regions such as the mid-estuary sand flats, Young's Bay, and Cathlamet Bay (correlation coefficient, $R \sim 0.2$–0.4; Fig. 8a). Winter wind speed correlates with surface turbidity in the mid-estuary and Young's Bay as well but also in Baker Bay (Fig. 8b; see Fig. 1 for place-names). The differences between summer and winter turbidity patterns in shallow water likely stem from seasonal differences in prevailing wind direction, fetch, and therefore local wave forcing. Winter winds primarily come from the east-southeast and therefore have a larger influence on turbidity in Baker Bay. By contrast, summertime winds are primarily west-northwesterly, such that their influence is concentrated along southern regions in the CRE. Note that although white-capping of wind-driven waves may influence the surface reflectance signal, evaluation of in situ data at

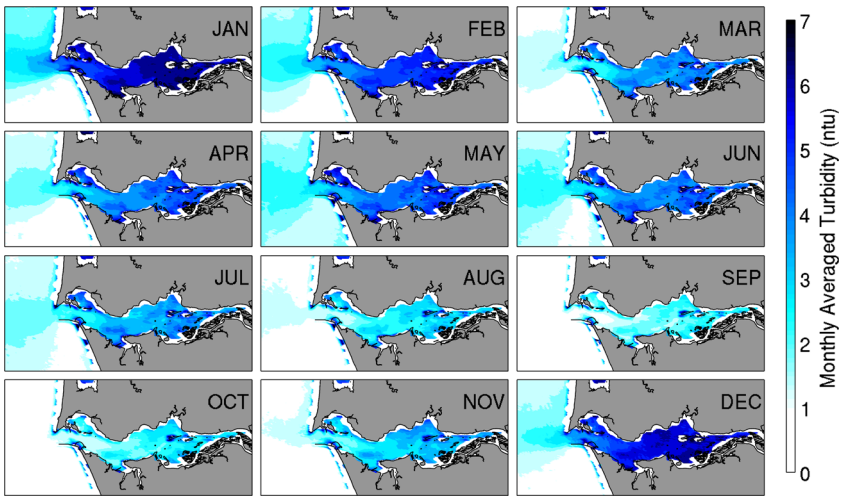

Fig. 7 Monthly averaged turbidity distributions. Elevated concentrations begin during the winter months and persist throughout the spring while high river flows are maintained. Minimum concentrations occur in late summer at periods of low flow. Each plot is the average of at least 65 MODIS images

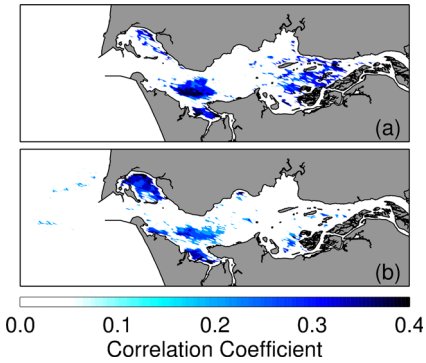

Fig. 8 Correlation map between MODIS derived turbidity and wind speed during summer (**a**) and winter (**b**). The effect of wind speed is confined to shallow locations and is greatest in the lower estuary bays. Summer time winds affect the southern bays, whereas wintertime winds mostly affect Baker Bay in the northern estuary near the mouth

Saturn 07 in Baker Bay confirms that turbidity increases during large wind events ($R \sim 0.5$, $N > 2000$).

Wave energy from ocean swell (period ≥10 s) correlates with surface turbidity estimates at the mouth of the CRE near the jetties ($R \sim 0.4$; Fig. 9), although we cannot evaluate whether the signal is due to white-capping from wave breaking, turbidity, or both. Nonetheless, we observe that the elevated MODIS reflectance at the jetties is consistent with observations that suggest that wave-induced erosion is an important factor in jetty evolution (e.g., Hickson and Rodolf 1950; Elias et al. 2012). Unlike other estuaries (e.g., Talke and Stacey 2008), the effect of ocean swell on turbidity cannot be statistically shown beyond the entrance, though some low-frequency wave energy likely propagates inland and to Baker Bay.

Greater diurnal tidal range, defined here as the difference between the daily maximum and minimum tidal elevations, is significantly correlated with turbidity throughout the system (median $R \sim 0.36$; Fig. 10). Since tidal currents increase during periods with large tidal range (spring tides), vertical eddy viscosity increases, stratification is reduced, and more sediment is mixed to the surface (Allen et al. 1980; Jay and Smith 1990a). The correlation between greater diurnal tidal range and turbidity is maximal in mid-estuary, where tidal-monthly variations in stratification and ETM concentration are greatest (Gelfenbaum 1983; Jay and Smith 1990a). The greater diurnal tidal range also shows a positive relationship with turbidity in the coastal ocean, consistent with previous studies that suggest more sediment is exported to the coast during spring tides

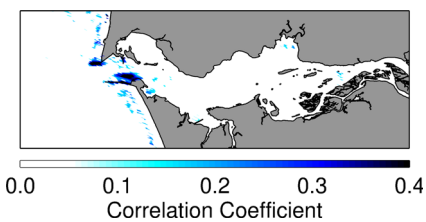

Fig. 9 Correlation map between MODIS-derived turbidity and ocean swell wave energy. Waves only affect turbidity near the mouth of the CRE

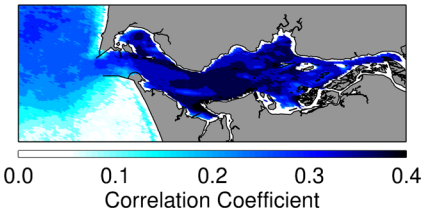

Fig. 10 Correlation map between MODIS derived turbidity and tidal range. Tidal range is positively correlated with surface turbidity throughout the system

when vertical mixing is amplified (Jay et al. 2007; Fain et al. 2001).

River flow is the most statistically significant process influencing variability in surface turbidity (Fig. 11). The total flow measured at the Beaver Army Terminal (Rkm 86), which measures an average of 97 % of the total freshwater flow at the mouth (Orem, 1968) and includes both the main stem Columbia and most major coastal tributaries, shows a median R of 0.51 over the estuary (Fig. 11). We find, however, that different tributaries exhibit statistically distinct influences on the CRE turbidity. Coastal tributaries such as the Willamette (lagged by 1 day) and the Cowlitz (lagged by 1 day) exhibit a dominant influence within the estuary, with median R of 0.71 and 0.63, respectively. The main stem Columbia River (measured with a 2-day lag from The Dalles) exhibits a much lower correlation within the estuary (median R of 0.29), despite carrying an average of 75 % of the total annual discharge.

Despite its weaker effect on surface turbidity levels, main stem Columbia River discharge is evidently large enough in May/June to make a significant impact on overall turbidity levels (Figs. 2 and 7); during this period, the discharge from coastal tributaries is relatively small. The relatively weak correlation between surface turbidity and main stem discharge is likely augmented by a combination of the main stem sediment supply (see below) and stratification during the Columbia River freshet that damps vertical mixing and therefore the observed surface signal. Moreover, the larger river discharge in May/June exports significant quantities of sediment to the shelf (Spahn et al. 2009), by increasing seaward advection, reducing the salinity containing volume of the estuary that can trap sediment, lowering the trapping efficiency (which is inverse to supply concentration), and decreasing suspended sediment residence time (Fain et al. 2001). Jay et al. (2007) provide a more complete discussion.

The influence of coastal tributaries, which are primarily driven by winter storm events (rain and sometimes rain-on-snow), helps explain why the largest turbidities are observed during winter (Fig. 7). Analysis of US Geological Survey water quality data and sediment concentration data indicates that the Willamette River sediment load typically has a higher percentage of fine sediment (with a strong influence on surface turbidity) than the load from the main stem (Naik and Jay 2011). Wind may also play a role in enhancing wintertime turbidity (Fig. 8).

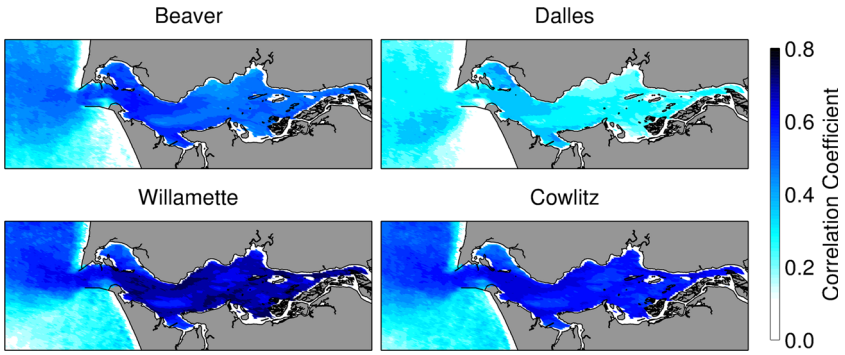

Fig. 11 Correlation map between MODIS-derived turbidity and river flow measured at Beaver Army Terminal, The Dalles, Willamette River, and Cowlitz River

The observed influence of different tributaries on CRE turbidity is consistent with local geology but is strongly influenced by the reservoir system (Naik and Jay 2010, 2011). As discussed by Gates (1994), the Lower Columbia River is thought to have been historically sediment-poor, possibly because late Pleistocene floods scoured much of the Columbia River Basin. By contrast, coastal tributaries such as the Cowlitz and Willamette carry runoff from regions with active volcanoes and fine alluvium and aeolian deposits (Theisen 1958; Balster and Parsons 1968). The Cowlitz, which drains the Mt. St. Helens watershed, has historically discharged large amounts of sediment to the CRE (Sherwood et al. 1990; Sherwood and Craeger 1990) and USGS measurements suggest elevated suspended sediment concentrations related to the eruption in May 1980 persist to this day (data not shown). Local development and land use practices may also affect coastal tributaries like the Willamette (Lyons and Beschta 1983; Naiman et al. 1992; Benner and Sedell 1997; Norman et al. 1998). Since 1937 and 1941, dams in both the Columbia and Willamette River Basins have increasingly curtailed sediment export (Naik and Jay 2011; Templeton and Jay 2013; Wentz et al. 1998). However, the high correlation of turbidity with the Willamette hydrograph suggests that significant amounts of turbidity enter the system during coastal storm events. Because the Willamette and Cowlitz may also act as a proxy for smaller, unregulated coastal streams, we conclude that coastal tributaries generally are important sources of suspended sediment exported to the estuary and the coastal ocean.

Turbidity Transects

We next examine the longitudinal distribution of turbidity along the North and South Channels as defined in Fig. 1. Example transects are shown during low/high flows (3000 and 11,000 $m^3\ s^{-1}$ with 500-$m^3\ s^{-1}$ window; Fig. 12a, b) and neap/spring tides (2.0 and 3.5 m with 0.15-m window;

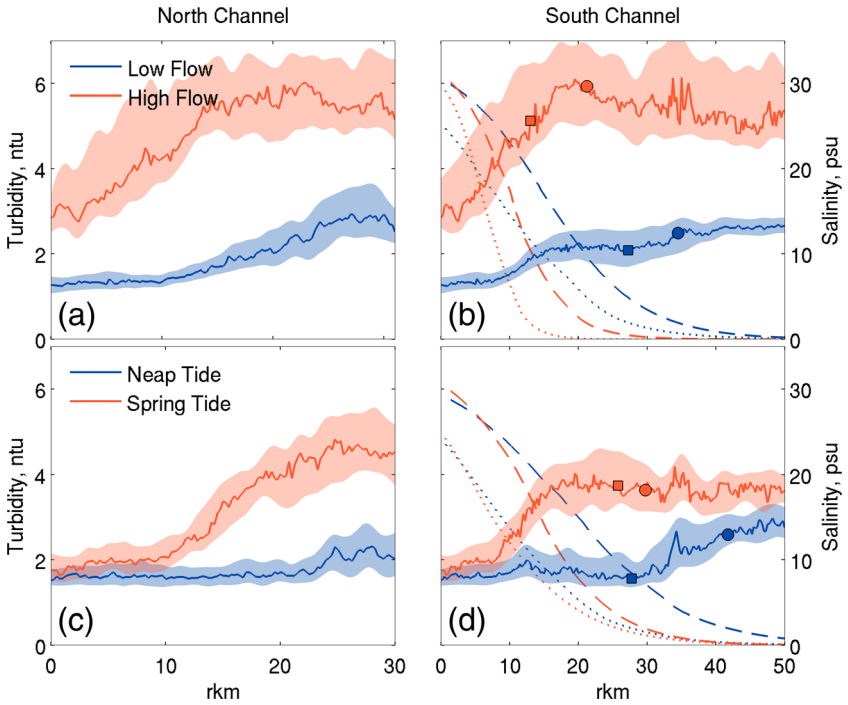

Fig. 12 Longitudinal transects of turbidity (*solid lines*) in the North (*left*) and South (*right*) Channels. *Transects* represent median values, binned according to greater diurnal tidal ranges (bottom; 2.5 and 3 m with 0.15-m window) and river flow (top; 3000 and 11,000 $m^3\ s^{-1}$ with 500-$m^3\ s^{-1}$ window). *Shaded regions* denote 33rd and 67th quantiles of binned transects. Near surface and near-bed salinity intrusion (*dotted* and *dashed lines*, respectively) and 2 psu contours (*squares* and *circles*, respectively) have paired response with turbidity distribution to forcing data

Fig. 12c, d). Note that transects exhibit variance around the median (illustrated by the 33rd and 67th quantiles as shaded regions in Fig. 12), which is a result of inherent variance of environmental conditions within the bin window and possibly uncorrected atmospheric artifacts in remote measurements. Tidal excursion of the ETM (~20 km; Gelfenbaum 1983) and time varying mixing also contribute to the variance because individual transects are observed during different tidal phases. Since a large number of data are concatenated in each bin (>50), we argue that the median curves in Fig. 12 approximate the tidally averaged turbidity distribution for each greater diurnal tidal range/river flow combination.

Asymmetry in Turbidity Transects

The MODIS-based turbidity transects show that turbidity distributions are typically asymmetrical, with larger gradients observed downstream of the maximum. For example, gradients of ~0.3 ntu km^{-1} are observed downstream of the ETM vs 0.15 ntu km^{-1} upstream of the ETM during large river discharge and large tides in the South Channel (Fig. 12). These observations qualitatively agree with theoretical studies of ETM behavior, which suggest that asymmetry can develop because different physical processes dominate sediment transport on either side of the maximum (Talke et al. 2008, 2009b). Landward of an ETM, upstream sediment fluxes are small and the turbidity distribution is set by factors such as river flow, dispersion, tidal pumping, and channel convergence. By contrast, the turbidity distribution seaward of the ETM is controlled by the same factors that produce the salinity field (Talke et al. 2008), resulting in similar longitudinal length scales of variation (e.g., as encapsulated in Eq. 1). The relationship between salinity and turbidity scales is observed in MODIS-based transects in the South Channel (Fig. 12d); during the transition from spring to neap, both the near-bed salinity field and the ETM move landward (increasing x_c in Eq. 1) and become stretched over a larger distance (increasing x_l in Eq. 1). High flow conditions (Fig. 12b) exhibit increased gradients in both the salinity and turbidity fields downstream of the ETM.

Asymmetry in surface turbidity during high flow conditions can be quantified by fitting a hyperbolic tangent curve to either side of the ETM (similar to Eq. 1 for the salinity field). Results confirm that asymmetry is especially prominent during high river flows as the ETM region approaches Rkm 15 in the North Channel and Rkm 20 in the South Channel (Fig. 12a, b); turbidity gradient length scales (x_L) are four to five times greater upstream of the ETM than downstream (Table 5). Because these locations have local depth maxima (Fig. 3) and landward sediment fluxes are enhanced with increasing channel depth (Talke et al. 2009b; de Jonge et al. 2014), topographic features may contribute to observed asymmetry.

Table 5 Turbidity gradient length scales downstream and upstream of the ETM in the North and South Channels during high river flows (Fig. 12a, b)

	Downstream of ETM	Upstream of ETM
North Channel	11.6 km	42.3 km
South Channel	11.8 km	55.7 km

Length scales are estimated by fitting hyperbolic tangent curve to turbidity upstream and downstream of the ETM

Response of ETM to River Flow and Tidal Forcing

The response of ETM magnitude and position to forcing data is examined with bin-median transects in the river flow (1000 m^3 s^{-1} window) and greater diurnal tidal range (0.25 m window) parameter space (Fig. 13). In both the North and South Channels, the magnitude of the ETM (C_{max}) is a function of greater diurnal tidal range and river flow. Surface C_{max} increases by a factor of 2–3 when flow rate increases from 2500 to 10,000 m^3 s^{-1} (Fig. 12c, d), with the largest increase occurring during neap tide conditions (Fig. 13). For the largest river discharge bin with extensive data available (10,000 m^3 s^{-1}), C_{max} is approximately constant regardless of greater diurnal tidal range. By contrast, turbidity values approximately double when tide range increases from 2 to 3.5 m during low flow conditions (<5000 m^3 s^{-1}). These observations are consistent with the hypothesis that local resuspension and mixing processes dominate sediment concentration magnitudes during low river discharge but that external sediment input from the river dominates estuarine sediment concentrations during large discharge events. We note that the background river turbidity of about 2 NTU during low discharge conditions (e.g., measured at Saturn 05 at Rkm 86) is significant relative to estuary conditions and may contribute to the observed C_{max}, particularly upstream of Rkm 40, where channel width converges and salinity is generally absent. The dilution of river water downstream of Rkm 40 during low discharge conditions (as measured by increasing salinity) may therefore contribute to the overall longitudinal profile observed in Fig. 12b, in which no clear maximum is observed and turbidity decreases all the way to the ocean boundary.

The location of the ETM (X_{max}) in the North Channel is fairly stable, between Rkm 20 and 25, for a majority (~55 %) of river discharge and tidal conditions (Fig. 13a). The possible exception is non-neap tides during low river discharge, in which X_{max} switches to an upstream locus between Rkm 25 and 30 (Figs. 12a and 13a). However, as shown in Fig. 12a, the statistical significance of the upstream movement is somewhat ambiguous. Since the ~10-km range over which X_{max} varies and turbidity is elevated is much smaller than the tidal excursion we conclude that the tidally averaged position of the North Channel turbid zone or ETM is relatively fixed for all conditions, at least to within the accuracy of our estimate.

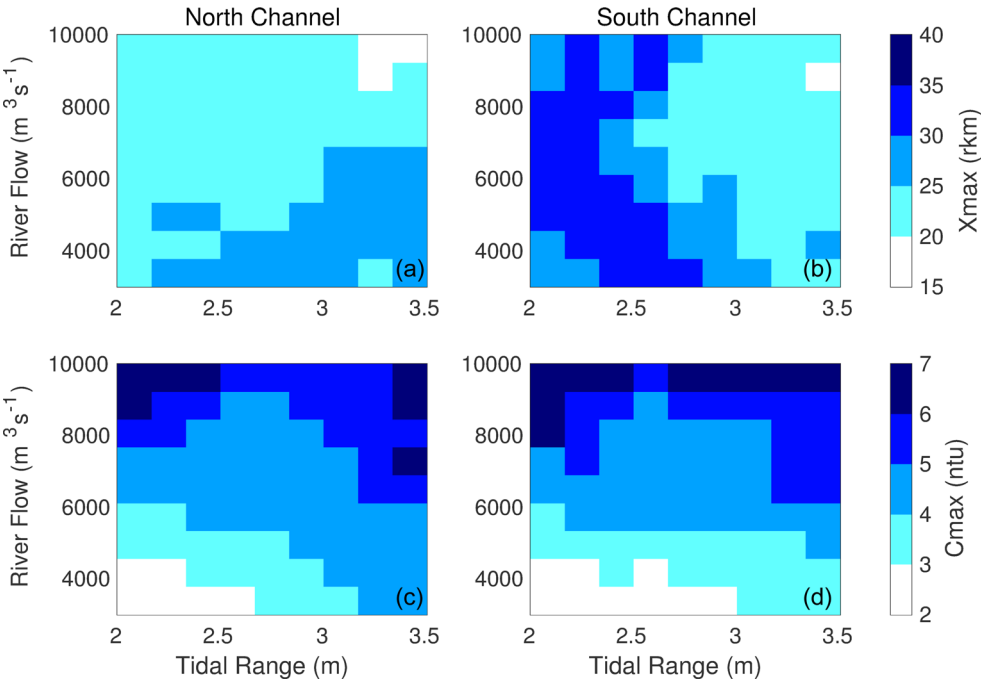

Fig. 13 The location (X_{max}) and magnitude (C_{max}) of the ETM in the North (*left*) and South (*right*) Channel plotted in the river flow and tidal range parameter space. Increasing river flow and tidal range promote seaward advection and greater intensity of the ETM

X_{max} in the South Channel is also found near Rkm 20–25 for a large proportion (49 %) of the river discharge and tidal range parameter space. Interestingly however, X_{max} exhibits a different dependency on tidal forcing in the South Channel than in the North Channel and is found further upstream (Rkm 30–35) as tidal range increases. During neap tides, reduced vertical mixing and higher stratification result in increased salinity intrusion and landward sediment transport (Gelfenbaum 1983; Jay and Smith 1990a; Talke et al. 2009a, b); similarly, reduced river flow results in the upstream movement of salinity and turbidity (Fig. 12). The South Channel X_{max} location is especially sensitive whenever tidal ranges are close to 2.7 m; X_{max} decreases by 5 km as tidal range exceeds 2.7 m for nearly all river discharges (Fig. 13b).

The location of the surface ETM is influenced by the stratification and mixing within the system and responds in concert with the salinity field to forcing data (Fig. 12). During spring tides, tidally averaged South Channel salinity intrusion (marked by the 2 PSU isohaline X_2) differs by <3 km at the surface and bed (Fig. 12d; compare positions of pink square and circle). Under these conditions, X_{max} is downstream of the near-bed X_2 and occurs near the 8-psu contour. By contrast, surface and bottom X_2 are separated by O (10 km) during neap tide conditions (Fig. 12d), indicating a strained salinity field and increased stratification. X_{max} is shifted landward of X_2 in this case and occurs near the 1-psu contour. For intermediate greater diurnal tidal ranges, South Channel X_{max} exhibits a behavior in between the spring and neap extremes for both small and large discharge (Fig. 12b).

Comparison of North and South Channels: Topographic Trapping

The North and South Channels exhibit different reactions to increased river discharge. While the South Channel salinity field and zone of stratification move downstream 10–15 km as river discharge increases (Figs. 12b and 14c, d), the North Channel remains stratified at Rkm 16 for all but the largest discharge conditions (>15,000 m^3 s^{-1}; Fig. 13a, b). This behavior occurs both because the North Channel receives less river discharge (Jay and Smith 1990a, b) and is thus less sensitive to changing flow conditions but also because of the topographic holes at Rkm 16 and Rkm 25 (Fig. 3) that trap saline water. Vertical mixing at Rkm 16 in the North Channel is thus nearly always inhibited to some degree, resulting in decreased surface turbidity compared to locations upstream. Strong stratification at Rkm 16 also implies vigorous landward bottom currents due to gravitational circulation (MacCready 2007) and internal asymmetry (Jay 2010), both of which scale as H^2 and strongly affect the ETM position (Jay 2010; Talke et al. 2008; Hudson 2014). The decrease in depth from ~16 to ~10 m on either side of Rkm 16 implies a twofold alteration in upstream circulation over a small distance (not accounting for altered eddy diffusivity) and is a barrier to downstream sediment transport. The South Channel salinity and turbidity fields are much more sensitive to altered river discharge than the North Channel but also exhibit evidence of persistent turbidity gradients downstream of the topographic holes at Rkm 20 during most flow and tidal conditions (Fig. 12b, d).

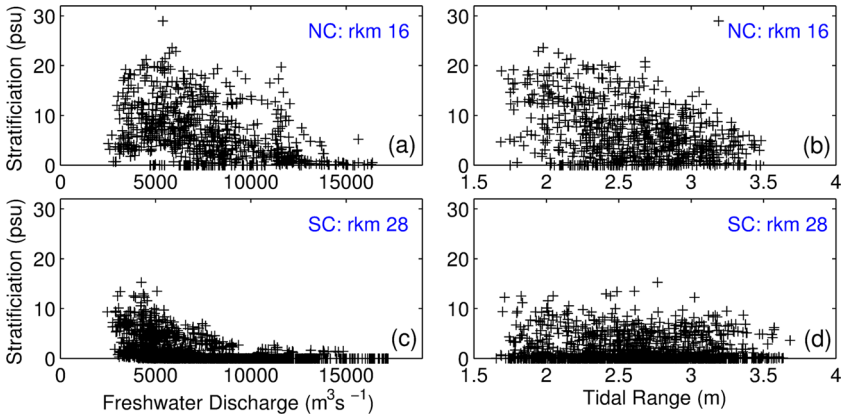

Fig. 14 Daily averaged stratification in the North (*top*) and South (*bottom*) Channel. At Rkm 16 stratification in the North Channel decreases with tidal range (*right*) and river flow (*left*). At Rkm 28, stratification in the South Channel decreases with freshwater discharge but depends little on tidal range

The scaling of estuarine circulation with depth supports the notion that trapping of turbidity occurs due to circulation patterns related to topography—i.e., due to "topographic trapping." To demonstrate this idea, we note that two features of the turbidity field are associated with the holes at Rkm 16 and 25 in the North Channel. First, a large gradient of turbidity occurs downstream of the hole at Rkm 16 in the North Channel, consistent with a strong gradient in salinity and landward transport. Observations of Jay et al. (2007) confirm that landward transport and trapping efficiency in the CRE ($E = C_{max} / C_R$; where C_R = river concentration of particles) are indeed greatest in the North Channel near Rkm 15. Second, sediment trapping appears to be fixed between the topographic holes at Rkm 16 and Rkm 25 for much of the greater diurnal tidal range/river flow parameter space (Figs. 12 and 13). Although the surface ETM appears to persist in this region, surface and bottom turbidity maximum may not be coincident (as with the salinity field in the South Channel) and further research is necessary.

Trapping Efficiency

Scaling and analysis of data from 15 systems (Jay et al. 2007) suggest that trapping efficiency, E, decreases as the supply number S_R increases:

$$S_R = \frac{U_R \, W_s}{U_T \kappa U_*} \tag{3}$$

where W_S is particle settling velocity, κ is von Karmann's constant, U_* is the shear velocity, U_R is river flow velocity, and U_T is the tidal flow velocity.

The Jay et al. (2007) scaling suggests that the following observations drive ETM behavior in the CRE:

- For constant river flow, supply number S_R increases and trapping efficiency E decreases during small (neap) tides, since weak tidal mixing during these times fails to move sediment from the bed. Fluvial sources of sediment may then represent the maximum concentrations in the system. Our results, in which relatively large concentrations are observed in the river relative to the ETM during neap conditions, are consistent with this interpretation (e.g., Fig. 12d).
- Conversely, large (spring) tides enhance vertical mixing in the estuary, local resuspension increases, and salinity intrusion decreases due to a reduction in estuarine circulation. These factors increase E, decrease S_R, and move the ETM downstream from the fluvial source (for the same river flow). Our results largely agree with this scaling (Fig. 12d).

Conclusions

In this study, MODIS-based surface reflectance measurements and in situ data were used to gain further insight into surface turbidity distributions and transport processes in the CRE. Because MODIS data are synoptic and span a considerable time frame (~15 years), a "big data" approach yields spatial and temporal insights not easily available from either in situ measurements or field cruises. More than 1500 images were used to develop a climatology of turbidity in the estuary and to quantitatively explore the processes that drive ETM behavior. Analyses of these images highlight the following conclusions:

1. Surface turbidity variations in the estuary are most strongly correlated with river flow; thus, monthly averaged concentrations are greatest during the winter months when river flows from turbid, coastal tributaries are maximum. Elevated turbidity persists, however, during the spring freshet in the main stem Columbia, and annual minimum turbidity levels are observed during late summer. Greater diurnal tidal range controls surface turbidity concentrations to second order. As a result, SSC is maximal and the ETM most prominent during spring tides when tidal currents and vertical mixing are elevated.

2. The synoptic nature of satellite data reveals two turbidity maxima in the CRE—one in the North Channel and one in the South Channel—with different responses to external forcing. Both ETM increase in magnitude with increasing river flow and tidal range. However, while the North Channel ETM location is relatively stable over the observed range of river flow and tidal range, the South Channel ETM migrates sea/landward about 20 km with increasing/decreasing river flow and tidal range.
3. Although turbidity levels fluctuate during the year, the spatial distribution is more consistent, and large gradients are often observed in the mid/lower estuary. MODIS-based turbidity transects also validate the theoretical expectation that ETM are inherently asymmetric. Because the distribution of sediment downstream of the ETM location (X_{max}) scales with salinity intrusion, and upstream of X_{max} with river discharge, an asymmetric profile can develop. In the CRE, turbidity gradients seaward of the ETM can reach twice those upstream of the ETM during large river flows and tidal ranges.
4. While large river flows and greater diurnal tidal ranges prompt seaward migration of the ETM, topographic trapping in mid-estuary near local depth maxima limits further downstream movement. Because internal asymmetry and gravitational circulation increase nonlinearly with water depth, they provide a mechanism for limiting ETM movement at this location.

These results highlight a fundamental characteristic of the CRE—since ETM are not observed seaward of topographic lows in the mid/lower estuary, and since asymmetry in the turbidity distribution increases as X_{max} approaches this region from upstream, bottom topography is likely an essential component contributing to sediment transport and ETM formation. Indeed, maximal values of trapping efficiency (E) occur in the North Channel at Rkm 15, near a local depression in the bed (Jay et al., 2007). Topographic trapping of ETM has also been observed in other estuaries (Roberts and Pierce 1976; Schoellhamer 2001; Ralston et al. 2012) and is therefore fundamental to the sediment dynamics in many estuarine systems—especially those with strong baroclinic gradients that drive depth-sensitive circulation. Despite considerable stratification in the mid/lower estuary (Figs. 12 and 14), our measurements indicate that surface signatures of topographic trapping can be observed with satellite data.

Acknowledgments This work was supported by the Office of Naval Research under award N00014-13-1-0084 and the National Science Foundation, Award number 1455350. We thank USGS, NOAA, NASA, and CMOP personnel for making their data available.

References

Allen, G.P., J.C. Salomon, P. Bassoullet, Y. Du Phenhoat, and C. De Grandpré. 1980. Effects of tides on mixing and suspended sediment transport in macrotidal estuaries. *Sedimentary Geology* 26: 69–90.

Balster, C. A. and R. B. Parsons. 1968. Geomorphology and soils Willamette Valley, Oregon. Soil Conservation Service, Special Report 265.

Benner, Patricia A., and James R. Sedell. 1997. Upper Willamette River landscape: a historic perspective. In *River quality: dynamics and resotoration*, eds. Antonius Laenen, and David A. Dunnette, 23–47. New York: CRC Press.

Bricaud, Annick, André Morel, and Louis Prieur. 1981. Absorption by dissolved organic matter of the sea (yellow substance) in the UV and visible domains. *Limonl. Oceaonogr.* 26: 43–53.

Bricaud, Annick, Marcel Babin, André Morel, and Herve Claustre. 1995. Variability in the chlorophyll-specific absorption coefficients of natural phytoplankton: analysis and parameterization. *Journal of Geophysical Research* 100(C7): 13,321–13,332.

Burchard, H., and H. Baumert. 1998. The formation of estuarine turbidity maxima due to density effects in the salt wedge. A hydrodynamic process study. *Journal of Physical Oceanography* 28(2): 309–321.

Burchard, H., H. Schuttelaars, and W. Geyer. 2013. Residual sediment fluxes in weakly-to-periodically stratified estuaries and tidal inlets. *Journal of Physical Oceanography* 43(9): 1841–1861.

Chawla, Arun, David A. Jay, Antonio M. Baptista, Michael Wilkin, and Charles Seaton. 2007. Seasonal variability and estuary–shelf interactions in circulation dynamics of a river-dominated estuary. *Estuaries and Coasts* 31(2): 269–288. doi:10.1007/s12237-007-9022-7.

Chen, Zhiqiang, Chuamin Hu, and Frank Muller–Karger. 2006. Monitoring turbidity in Tampa Bay using MODIS/Aqua 250–m imagery. *Remote Sensing of Environment* 109: 207–220.

Chernetsky, A.S., H.M. Schuttelaars, and S.A. Talke. 2010. The effect of tidal asymmetry and temporal settling lag on sediment trapping in tidal estuaries. *Ocean Dynamics* 60: 1219–1241. doi:10.1007/s10236-010-0329-8.

Christie, M.C., K.R. Dyer, and P. Turner. 1999. Sediment flux and bed level measurements from a macro tidal mudflat. *Estuarine, Coastal and Shelf Science* 49: 667–688.

de Jonge, V.N., and J.E.E. van Beusekom. 1995. Wind and tide induced resuspension of sediment and microphytobenthos from tidal flats in the Ems estuary. *Limnology and Oceanography* 40: 766–778.

de Jonge, V.N., Henk M. Schuttelaars, Justus E.E. van Beusekom, Stefan A. Talke, and Huib E. de Swart. 2014. The influence of channel deepening on estuarine turbidity levels and dynamics, as exemplified by the Ems estuary. *Estuarine, Coastal and Shelf Science* 139: 46–59.

de Swart, H.E., H.M. Schuttelaars, and S.A. Talke. 2009. Initial growth of phytoplankton in turbid estuaries: a simple model. *Continental Shelf Research* 29(1): 136–147.

Donker, Jasper J.A., and Huib de Swart. 2013. Effects of bottom slope, flocculation and hindered settling on the coupled dynamics of currents and suspended sediment in highly turbid estuaries, a simple model. *Ocean Dynamics* 63: 311–327.

Doxaran, David, Jean-Marie Friodefond, and Patrice Castaing. 2003. Remote-sensing reflectance of turbid sediment-dominated waters. Reduction of sediment type variations and changing illumination conditions effects by the use of reflectance ratios. *Applied Optics* 42: 2623–2634.

Doxaran, David, Castaing Patrice, and S.J. Lavender. 2006. Monitoring the maximum turbidity zone and detecting fine-scale turbidity features in the Gironde estuary using high spatial resolution satellite sensor (SPOT HRV, Landsat ETM+) data. *International Journal of Remote Sensing* 27: 2303–2321.

Doxaran, David, Jean-Marie Friodefond, Patric Castaing, and Marcel Babin. 2009. Dynamics of the turbidity maximum zone in a macrotidal estuary (the Gironde, France): observations from field and MODIS satellite data. *Estuarine, Coastal and Shelf Science* 81: 321–332. doi:10.1016/j.ecss.2008.11.013.

Elias, E.P.L., G. Gelfenbaum, and A.J. Van der Westhuysen. 2012. Validation of a coupled wave-flow model in a high-energy setting: the mouth of the Columbia River. *Journal of Geophysical Research* 117: C09011. doi:10.1029/2012JC008105.

Fain, Annika M.V., David A. Jay, Doug J. Wilson, Phil M. Orton, and Antonio M. Baptista. 2001. Seasonal and tidal monthly patterns of particulate matter dynamics in the Columbia River Estuary. *Estuaries* 24: 770–786.

Festa, John F., and Donald V. Hansen. 1978. Turbidity maxima in partially mixed estuaries: a two–dimensional numerical model. *Estuarine and Coastal Marine Science* 7: 347–359.

Gates, Edward Breed. 1994. The holocene sedimentary framework of the lower Columbia River basin. Masters thesis, Portland State University.

Gelfenbaum, Guy. 1983. Suspended-sediment response to semidiurnal and fortnightly tidal variations in a mesotidal estuary: Columbia River, USA. *Marine Geology* 52: 39–57.

Geyer, W. Rockwell. 1993. The importance of suppression of turbulence by stratification on the estuarine turbidity maximum. *Estuaries* 16: 113–125.

Geyer, W. Rockwell, Jonathan D. Woodruff, and Peter Traykovski. 2001. Sediment transport and trapping in the Hudson River Estuary. *Estuaries* 24(5): 670–679.

Hansen, D.V., and M. Rattray Jr. 1965. Gravitational circulation in straits and estuaries. *Journal of Marine Research* 23: 104–122.

Hickey, B.M., R.M. Kudela, J.D. Nash, K.W. Bruland, W.T. Peterson, P. MacCready, E.J. Lessard, D.A. Jay, N.S. Banas, A.M. Baptista, E.P. Dever, P.M. Kosro, L.K. Kilcher, A.R. Horner-Devine, E.D. Zaron, R.M. McCabe, J.O. Peterson, P.M. Orton, J. Pan, and M.C. Lohan. 2010. River influences on shelf ecosystems: introduction and synthesis. *Journal of Geophysical Research* 115: C00B17. doi:10.1029/2009JC5452.

Hickson, R. E. and F. W. Rodolf. 1950. History of Columbia River jetties. In Proceedings of the first conference on coastal engineering, ed. J. W. Johnson, 283–298.

Horner–Devine, Alexander R., David A. Jay, Phillip M. Orton, and Emily Y. Spahn. 2009. A conceptual model of the strongly tidal Columbia River plume. *Journal of Marine Systems* 78: 460–475. doi:10.1016/j.jmarsys.2008.11.025.

Hu, Chuanmin, Zhiqiang Chen, Tonya D. Clayton, Peter Swarzenski, John C. Brock, Frank E. Juller, and Karger. 2004. Assessment of estuarine water-quality indicators using MODIS medium-resolution bands: initial results from Tampa Bay, FL. *Remote Sensing of Environment* 93: 423–441. doi:10.1016/j.res.2004.08.007.

Hudson, Austin S. 2014. Applications of remote sensing to the study of estuarine physics: suspended sediment dynamics in the Columbia River Estuary. Masters thesis, Portland State University.

Hughes, F.W., and M. Rattray Jr. 1980. Salt flux and mixing in the Columbia River Estuary. *Estuarine and Coastal Marine Science* 10: 479–493.

IOCCG. 2006. Remote sensing of inherent optical properties: fundamentals, tests of algorithms, and applications. In *Reports of the International Ocean-Colour Coordinating Group, No. 5*, ed. Z.-P. Lee. Dartmouth, Canada: IOCCG.

Jay, David A. 1984. *Circulatory processes in the Columbia River Estuary.* Astoria, Oregon: CREST.

Jay, David A. 1991. Green's law revisited: tidal long-wave propagation in channels with strong topography. *Journal of Geophysical Research* 96(C11): 20,585–20,598.

Jay, David A. 2010. Estuarine variability. In *Contemporary issues in estuarine physics*, ed. Arnoldo Valle-Levinson, 62–99. New York: Cambridge University Press.

Jay, David A., and Jeffery D. Musiak. 1994. Particle trapping in estuarine tidal flows. *Journal of Geophysical Research* 99(C10): 20,445–20,461.

Jay, David A., and Jeffery D. Musiak. 1996. Internal tidal asymmetry in channel flows: origins and consequences. *Coastal and Estuarine Studies* 50: 211–249.

Jay, David A., and J. Dungan Smith. 1990a. Circulation, density distribution and neap–spring transitions in the Columbia River Estuary. *Progress in Oceanography* 25: 81–112.

Jay, David A., and J. Dungan Smith. 1990b. Residual circulation in shallow estuaries 1. Highly stratified, narrow estuaries. *Journal of Geophysical Research* 95(C1): 711–731.

Jay, David A., Benjamin S. Giese, and Christopher R. Sherwood. 1990. Energetics and sedimentary processes in the Columbia River Estuary. *Progress in Oceanography* 25: 157–174.

Jay, David A., Phillip M. Orton, David J. Kay, Annika Fain, and Antonio M. Baptista. 1999. Acoustic determination of sediment concentrations, settling velocities, horizontal transports and vertical fluxes in estuaries. *Porceedings of the IEEE Sixth Working Conference*: 258–263.

Jay, David A., Phillip M. Orton, Thomas Chisholm, Douglas J. Wilson, and Annika M.V. Fain. 2007. Particle trapping in stratified estuaries: application to observations. *Estuaries and Coasts* 30(6): 1106–1125.

Jay, D. A., S. A. Talke, A. Hudson, M. Twardowski. 2015. Estuarine turbidity maxima revisited: instrumental approaches, remote sensing, modeling studies, and new directions. In: Developments in sedimentology: fluvial-tidal sedimentology, eds. Philip J. Ashworth, James L. Best, and Daniel R. Parsons, 49–109: Elsevier.

Kappenberg, Jens, and Iris Grabemann. 2001. Variability of the mixing zones and estuarine turbidity maxima in the Elbe and Weser Estuaries. *Estuaries* 5: 699–706.

Lehner, Susanne, Ivonne Anders, and Gerhard Gayer. 2004. High resolution maps of suspended particulate matter concentration in the Geman Bight. *EARSeL eProceedings* 3: 118–126.

Lyons, Joseph K., and Robert L. Beschta. 1983. Land use, floods, and channel changes: Upper Middle Fork Willamette River, Oregon (1936-1980). *Water Resources Research* 19(2): 463–471.

MacCready, Parker. 2007. Estuarine adjustment. *Journal of Physical Oceanography* 37(8): 2133–2145.

Maritorena, Stéphane, David A. Siegel, and Alan R. Peterson. 2002. Optimization of semianalytical ocean color model for global-scale applications. *Applied Optics* 41(15): 2705–2714.

May, C.L., J.R. Koseff, L.V. Lucas, J.E. Cloern, and D.H. Schoellhamer. 2003. Effects of spatial and temporal variability of turbidity on phytoplankton blooms. *Marine Ecology Progress Series* 254: 111–128.

Meade, Robert H. 1969. Landward transport of bottom sediments in estuaries of the Atlantic coastal plain. *Journal of Sedimentary Research* 39(1): 222–234.

Naik, Pradeep K., and David A. Jay. 2010. Human and climate impacts on Columbia River hydrology and salmonids. *River Research and Applications* 27: 1270–1276. doi:10.1002/rra.1422.

Naik, Pradeep K., and David A. Jay. 2011. Distinguishing human and climate influences on the Columbia River: changes in mean flow and sediment transport. *Journal of Hydrology* 404: 259–277. doi:10.1016/j.jhydrol.2001.04.035.

Naiman, Robert J., Timothy J. Beechie, Lee E. Benda, Dean R. Berg, Peter A. Bison, Lee H. MacDonald, Matthew D. O'Connor, Patricia L. Olson, and E. Ashley Steel. 1992. Fundamental elements of ecologically healthy watersheds in the pacific northwest coastal ecoregion. In *Watershed management: balancing sustainability with environment change*, ed. R.J. Naiman, 127–188. New York: Springer-Verlag.

Neukermans, G., H. Liosel, X. Meriaux, R. Astoreca, and D. McKee. 2012. In situ variability of mass-specific beam attenuation and

backscattering of marine particles with respect to particle size, density, and composition. *Limnology and Oceanography* 57(1): 124–144.

Norman, David K., Jeff C. Cederholm, and William S. Lingley Jr. 1998. Flood plains, salmon habitat, and sand and gravel mining. *Washington Geology* 26(2): 1–28.

Orem, Hollis M. 1968. Discharge in the lower Columbia River basin, 1928–65. U.S. Geological Survey Circular 550.

Palacios, L. Sherry, Tawnya D. Peterson, and Raphael M. Kudela. 2009. Development of synthetic salinity from remote sensing for the Columbia River Plume. *Journal of Geophysical Research* 114: C00B05. doi:10.1029/2008JC004895.

Postma, H., and K. Kalle. 1955. Die Entstehung von Trübungszonen im Unterlauf der Flüsse, speziell im Hinblick auf die Verhältnisse in der Unterelbe. *Deutsche Hydrografische Zeitschrift* 8(4): 134–144.

Pruter, A.T., and D.L. Alverson. 1972. *The Columbia River Estuary and adjacent ocean waters*. Seattle: University of Washington Press.

Ralston, David K., W. Rockwell Geyer, and John C. Warner. 2012. Bathymetric controls on sediment transport in the Hudson River estuary: lateral asymmetry and frontal trapping. *Journal of Geophysical Research* 117: C10013. doi:10.1029/2012JC008124.

Reed, D.J., and J. Donovan. 1994. The character and composition of the Columbia River estuarine turbidity maximum. In *Changes in fluxes in estuaries: implications from science to management*, eds. K.R. Dyer, and Robert J. Orth, 445–450. Fredensborg, Denmark: Olsen and Olsen.

Roberts, W.P., and J.W. Pierce. 1976. Deposition in Upper Patuxent Estuary, Maryland, 1968-1969. *Estuarine and Coastal Marine Science* 4: 267–280.

Ruhl, C.A., D.H. Schoellhamer, R.P. Stumpf, and C.L. Lindsay. 2001. Combined use of remote sensing and continuous monitoring to analyse the variability of suspended–sediment concentrations in San Francisco bay, California. *Estuarine, Coastal, and Shelf Science* 53: 801–812.

Schoellhamer, D. H. 2001. Influence of salinity, bottom topography, and tides on locations of estuarine turbidity maxima in northern San Francisco Bay. In: Coastal and estuarine fine sediment transport processes, ed. McAnally, W.H., and Mehta, A.J., 343–357. Elsevier Science B.V.

Sherwood, Christopher R., and Joe S. Craeger. 1990. Sedimentary geology of the Columbia River Estuary. *Progress in Oceanography* 25: 15–79.

Sherwood, Christopher R., David A. Jay, R. Bradford Harvey, Peter Hamilton, and Charles A. Simenstad. 1990. Historical changes in the Columbia River Estuary. *Progress in Oceanography* 25: 299–352.

Simenstad, Charles A., Lawrence F. Small, and C. David McIntire. 1990. Consumption processes and food web structure in the Columbia River Estuary. *Progress in Oceanography* 25(1–4): 271–297.

Simpson, J.H., J. Brown, J. Matthes, and G. Allen. 1990. Tidal straining, density currents, and stirring in the control of estuarine stratification. *Estuaries* 13(2): 125–132.

Spahn, Emily Y., Alexander R. Horner-Devine, Jonathan D. Nash, David A. Jay, Levi Kilcher. 2009. Particle resuspension in the Columbia River plume near field. Journal of Geophysical Research: Oceans 114(C2).

Stevenson, J. Court, Michael S. Kearney, and Edward C. Pendleton. 1985. Sedimentation and erosion in a Chesapeake Bay brackish marsh system. *Marine Geology* 67(3): 213–235.

Talke, S.A., and M.T. Stacey. 2003. The influence of oceanic swell on flows over an estuarine intertidal mudflat in San Francisco Bay. *Estuarine, Coastal, and Shelf Science* 58: 541–554.

Talke, S.A., and M.T. Stacey. 2008. Suspended sediment fluxes at an intertidal flat: shifting influence of wave, wind, tidal, and freshwater forcing. *Continental Shelf Research* 28(6): 710–725. doi:10.1016/j.csr.2007.12.003.

Talke, S.A., H.E. de Swart, and H.M. Schuttelaars, 2008. An analytical model of the equilibrium distribution of suspended sediment in an estuary. In *Dohmen-Janssen and Hulscher, eds: River, coastal and estuarine morphodynamics 2008*, p. 403–411, London, Taylor and Francis.

Talke, S.A., H.E. de Swart, and V.N. de Jonge. 2009a. An idealized model and systematic process study of oxygen depletion in highly turbid estuaries. *Estuaries and Coasts* 32(4): 602–620.

Talke, S.A., H.E. De Swart, and H.M. Schuttelaars. 2009b. Feedback between residual circulation and sediment distribution in highly turbid estuaries: an analytical model. *Continental Shelf Research* 29(1): 119–135. doi:10.1016/j.csr.2007.09.002.

Templeton, W.J., and David A. Jay. 2013. Lower Columbia River sand supply and removal: estimates of two sand budget components. *Journal of Waterway, Port, Coastal, and Ocean Engineering* 139: 383–392.

Theisen, Arthur Albert. 1958. Distribution and characteristics of loess-like soil parent material in Northwestern Oregon. Masters Thesis, Oregon State College.

Uncles, R.J., J.A. Stephens, and R.E. Smith. 2002. The dependence of estuarine turbidity on the tidal intrusion length, tidal range and residence time. *Continental Shelf Research* 22: 1835–1856.

Vermote E. F. and A. Vermeulen. 1999. MODIS algorithm technical background document, atmospheric correction algorithm: spectral reflectances (MOD09). NASA.

Warner, John C., W. Rockwell Geyer, and James A. Lerczak. 2005. Numerical modeling of an estuary: a comprehensive skill assessment. *Journal of Geophysical Research* 110: C05001. doi:10.1029/2004JC002691.

Wentz, Denis A., Bernadine A. Bonn, Kurt D. Carpenter, Stephen R. Hinkle, Mary L. Janet, Frank A. Rinella, Mark A. Uhrich, Ian R. Waite, Antonius Laenen, Kenneth E. Bencala. 1998. Water quality in the Willamette Basin, Oregon, 1991–95. U.S. Geological Survey Circular 1161.